Chapter 2
Surface Plasmons for Chiral Sensing

Sotiris Droulias and Lykourgos Bougas

Abstract Chiral sensitive techniques have been used to probe the fundamental symmetries of the universe, study biomolecular structures, and even develop safe drugs. The traditional method for the measurement of chirality is through optical activity, however, chiroptical signals are inherently weak and often suppressed by large backgrounds. Different techniques have been proposed to overcome the limitations of traditionally used optical polarimetry, such as cavity- and/or nanophotonic-based schemes. In this chapter we demonstrate how surface plasmon resonance can be employed as a new research tool for chiral sensing, which we term here as CHIral Surface Plasmon Resonance (CHISPR). We present how surface plasmons at a metal-chiral interface are sensitive to the chirality parameter of the chiral medium and how their properties can be exploited to reveal information not easily accessible using standard polarimetric/nanophotonic approaches. We then present an experimental realisation of CHISPR, an angle-resolved measurement scheme, and demonstrate how can one detect the complete chirality (handedness and magnitude) of a chiral sample while being also sensitive to both the real and imaginary part of a chiral sample's refractive index. We present analytical results and numerical simulations of CHISPR measurements, predicting signals in the mdeg range for chiral samples of <100 nm thickness at visible wavelengths. Finally, we present a theoretical analysis that clarifies the underlying physics of the near-field chiral interactions and their far-field manifestation. In overall, CHISPR builds upon the strengths of standard SPR: does not require elaborate fabrication and has the advantage of being directly implementable on existing SPR instrumentation, making it, thus, an ideal modality for studying chirality dynamics on surfaces.

S. Droulias (✉)
Institute of Electronic Structure and Laser, FORTH, 71110 Heraklion, Crete, Greece
e-mail: sdroulias@iesl.forth.gr

L. Bougas (✉)
Institut für Physik, Johannes Gutenberg-Universität Mainz, 55128 Mainz, Germany
e-mail: lybougas@uni-mainz.de

E. Kamenetskii (ed.), *Chirality, Magnetism and Magnetoelectricity*,
Topics in Applied Physics 138,
https://doi.org/10.1007/978-3-030-62844-4_2

2.1 Introduction

Chirality, the geometric property of an object that is non-superimposable with its mirror image, is a foundational property of life: the weak interaction between fundamental particles violates parity [1]; biomolecular structures fundamental to life, such as amino acids, sugars, RNA and DNA, are both chiral and single-handed (i.e. homochiral) [1]; the chemistry of life and the functionalities of its building blocks are largely stereospecific [2]; organisms ranging from protists to plants and animals possess morphological asymmetries with respect to their left-right axis [3]. The development of sensitive chiral sensitive techniques has, therefore, been vital for this wide range of scientific disciplines, and has enabled the study of fundamental symmetries of the universe [4], determination of biomolecular structures [5–7], and even the development of safe and effective drugs [8, 9], to name few of its most prominent applications.[1]

2.1.1 Chirality and Optical Activity

Starting from the observation by Arago in 1811 of colours in the sunlight as seen through the optic axis of a quartz crystal placed between crossed polarizers, and the observation of optical rotation in organic liquids such as lemon oils and turpentine by Biot in 1815, the polarimetric techniques of optical rotatory dispersion (ORD) and circular dichroism (CD) have remained as the most widely used research tools in science for chiral sensing [11]. By 1825, Fresnel had discovered that linearly polarized light can be regarded as a superposition of the two possible forms of circularly polarized light [right (RCP) and left (LCP)], which lead to his proposal of the first phenomenological theory about optical activity, i.e. the ability of a chiral medium to rotate linearly polarized light travelling through it. His theory correctly attributed this effect to the propagation at different speeds in the *optically active* medium of the left- and right-circularly polarized components of the incident linearly polarized light. The expression for optical activity as proposed by Fresnel has the general form:

$$\varphi = \frac{\pi l}{\lambda}(n_- - n_+), \tag{2.1}$$

where $n_\pm$ are the (complex) indices of refraction of a chiral medium for RCP and LCP light, respectively, λ is the vacuum wavelength of light, and l the length of the medium.

With the advent of electromagnetism, a description of natural optically active materials on the macroscopic level became possible and is now contained in the

[1] Portions of this chapter have been reprinted with permission from [10]. Copyright 2019 American Chemical Society.

material parameters of the constitutive relations. In particular, these, along with Maxwell's equations, can be written as (according to Condon [12, 13], in the $e^{-i\omega t}$ convention):

$$\nabla \times \mathbf{E} = i\omega\mathbf{B}, \tag{2.2}$$

$$\nabla \times \mathbf{H} = -i\omega\mathbf{D}, \tag{2.3}$$

$$\mathbf{D} = \epsilon_0\epsilon_r\mathbf{E} + i\,(\kappa/c)\mathbf{H}, \tag{2.4}$$

$$\mathbf{B} = \mu_0\mu_r\mathbf{H} - i\,(\kappa/c)\mathbf{E}, \tag{2.5}$$

where ϵ_0, μ_0 are the vacuum permittivity and permeability, ϵ_r, μ_r the relative material permittivity and permeability, respectively, and c is the vacuum speed of light; κ is the chirality (also known as 'Pasteur') parameter, which expresses the chiral molecular response. The eigenwaves of such a medium are RCP/LCP (or $\pm$) waves, which propagate with refractive indices $n_\pm = n_c \pm \kappa$, respectively, where $(n_+ + n_-)/2 = n_c \equiv \sqrt{\epsilon_r\mu_r}$ is the average (background) refractive index.

Considering all the above, we can now see that $\varphi = (2\pi l/\lambda)\cdot\kappa$, and that the real part of κ, i.e. Re(κ), is associated with effects of circular birefringence, while the imaginary part of κ, Im(κ), with circular dichroism.

2.1.2 Chiral Sensing Techniques

The polarimetric techniques of ORD and CD allow for the direct detection of the real part and the imaginary part of φ, and, thus, of the chirality parameter κ of a natural optically active medium. A typical ORD/CD spectro-polarimeter generally consists of a light source, a set of polarizers for state preparation and analysis, and a spectral analysis and detection stage. Yet, two separate instruments are actually designed to perform, *separately*, ORD and CD measurements. Only in the recent years, new approaches towards generalized polarimetry, such as the technique of Mueller Matrix polarimetry, have been demonstrated, which enable a complete characterization of the optical properties of a medium and the simultaneous detection of both its circular birefringence and dichroism [14]. Notwithstanding, spectropolarimetry is being extensively used in basic research and remains the established analytical technique for quality and process control in the pharmaceutical, chemical, and agricultural industries. Despite their extensive use, though, the sensitivity limits of commercially available optical spectro-polarimeters, circular dichroism and optical rotation modules, are at the ~10–100 μdeg levels corresponding to analyte concentration detection limits at the (sub)-micromolar levels, constraining, thus, the extension of polarimetry to a wide range of important research and industrial applications that require improved sensitivity levels (e.g. sub-nM sensitivities). To overcome the limitations of traditional polarimetry in chiral sensing, different techniques have been proposed in the recent years. These techniques, which aim to enhance the matter-wave chiral

interaction, can in principle be arranged into two main categories, as they rely mainly on either *(a)* path-length enhancement or *(b)* chiral-field enhancement.

Path-length enhancement techniques typically rely on the use of optical mirrors to create either multipass cells or optical cavities, where in both cases spectropolarimetric signals are enhanced by the average number of passes through the medium. Multipass cells [15, 16] are technically easy to construct and implement, and optical path-length enhancements as large as $\times 500$ have been demonstrated [17, 18]; crucially though, multipass techniques cannot be, in principle, employed for the measurement of optical activity (owing to the effective round-trip cancellation of the polarization effects [19]). The solution is to use stable optical cavities [20–24], with which one can achieve path-length enhancements of up to 10^5 using state-of-the-art high quality mirrors, with effective path-lengths of up to several hundred kilometers (one needs to compare this to the 10 cm-long sample cell in a single-pass commercial polarimeter), enabling record sensitivities for measurements of absorption and birefringence (CD and ORD, respectively). Importantly, optical cavities can easily be made compact and allow for wave-matter interactions in small volumes. However, cavity-enhanced techniques become inadequate in systems with losses originating from absorption and/or scattering (e.g. chiral molecules within complex matrices, thin films, liquid and/or solid systems), because losses hinder the path-length enhancement. For the case of CD, in particular, path-length enhancement techniques can be mainly used to probe weak molecular transitions [20, 22, 25].

Chiral-field-enhancement techniques rely primarily on generating probing electromagnetic fields with chiral densities higher than circularly polarized plane waves, i.e. *superchiral* fields [26–32]. Chiral and/or achiral nanophotonic systems, such as plasmonic/dielectric nanostructures and metamaterials, can generate contorted intense near-fields with high chiral densities around a resonance frequency of the nanosystem, thus, amplifying the chiral-chiral interactions between them and a molecule. In general, nanophotonic approaches have proven to be a powerful means for granting access to weak chiroptical signals not previously attainable with traditional polarimetric techniques, however, the general principle of operation behind (almost) all contemporary nanophotonic chiral-sensing approaches primarily relies on the detection of enhanced CD signals in the presence of an optically active chiral substance. To achieve this, right- and left-circularly polarized waves are used to excite the system and generate these superchiral fields, and enable the ability to perform CD measurements in transmission. While several works have attributed the resulting CD signal to be proportional only to the imaginary part of the chirality parameter, i.e. $\mathrm{Im}(\kappa)$ (see, e.g., [31–33]), in reality, as supported by past and recent experimental and theoretical results [34–37] the observed CD signals depend on both the real and the imaginary part of κ [$\mathrm{Re}(\kappa)$ and $\mathrm{Im}(\kappa)$, respectively]. Thus, with most contemporary nanophotonic approaches, sensing of the magnitude and sign of both the real and imaginary part of the chirality parameter of a natural optically active substance (*complete* measurement) has not been possible, while elaborate fabrication is required and the employed nanosystems typically have intrinsic chiroptical responses that contribute to the total signal, often precluding direct quantitative measurement of chirality [26–31].

Considering, therefore, the importance of chiral sensing in research, it is vital to develop alternative schemes that overcome the above-mentioned limitations of path-length enhancement and/or chiral-field enhancement techniques. In particular, it is apparent that a general chiral sensing scheme should be able to discriminate between the contributions of $\mathrm{Re}(\kappa)$ and $\mathrm{Im}(\kappa)$, especially far from the chiral molecular resonances, where $\mathrm{Im}(\kappa)$ is weak and $\mathrm{Re}(\kappa)$ is dominant. Additionally, it should be sensitive to both the magnitude of the chirality parameter, $|\kappa|$, and its sign $\mathrm{sgn}(\kappa)$, as $|\kappa|$ is a function of the molecular properties (i.e. polarizability) and its concentration, while $\mathrm{sgn}(\kappa)$ depends on the handedness of the medium.

In this chapter we discuss how surface plasmon resonance (SPR) allows for the complete measurement of chirality (handedness and magnitude) of a chiral system. SPR has become an important technology in the areas of biochemistry, biology, and medical sciences because of its real-time, label-free, and noninvasive nature (see, e.g., [38, 39]). We demonstrate how chiral-sensitive SPR, i.e. CHISPR, is able to quantitatively detect both the real and imaginary part of the refractive index of a chiral substance (responsible for the refraction and absorption, respectively), contrary to most demonstrations that employ nanophotonic structures. We show that CHISPR is particularly suitable for chiral sensing from thin samples which are not easily measurable using alternative polarimetric techniques, and that it makes use of the advantage of being applicable directly on existing SPR instrumentation without the need for additional elaborate fabrication.

2.2 Surface Plasmon Resonance (SPR)

Surface plasmon resonance (SPR) refers to the resonant excitation of a surface plasmon polariton (SPP) at the interface between a metal and a dielectric (or, in general, between two materials, one with negative and one with positive permittivity). SPPs, in particular, are electromagnetic excitations that propagate along the metal-dielectric interface and are evanescently confined in the perpendicular direction. They involve the collective oscillation of conduction electrons at the surface of the metal (hence the term '*surface plasmon*') and they arise via the coupling of the electromagnetic fields to the surface plasmon (hence the term '*polariton*'). SPPs are TM (or '*p*')-polarized waves, i.e., their magnetic field lies entirely on the metal-dielectric interface.

SPR is the basis for many biosensor applications and different lab-on-a-chip sensors, owing to the sensitive dependence of the SPP characteristics on the permittivity of the dielectric region extending over the metal. In essence, slight changes in the permittivity of the dielectric lead to different propagation characteristics in the SPP and therefore a frequency shift in its resonance. By measuring such frequency shifts, one can detect the material changes occurring at the metal-dielectric interface.

Typical SPR setups involve a thin metallic layer (usually Ag or Au in the order of 50 nm) placed directly on a glass substrate, as shown in Fig. 2.1a in the well-known Kretschmann configuration (see [40, 41] for other customary setups). In this configuration the metallic layer extends along the xy-plane and SPP propagates along

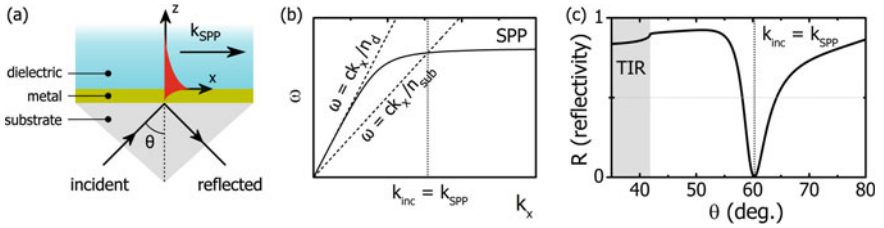

Fig. 2.1 SPR principle of operation. **a** Experimental implementation for SPR measurements (Kretschmann configuration). **b** Explanation of SPP excitation. The glass substrate is used to provide the necessary tangential wavenumber (k_{inc}) to match that of the SPP (k_{SPP}). This is shown as a crossing between the SPP dispersion (solid) and the light line in glass (dashed) (the light line in the dielectric is also shown). **c** Excitation of surface plasmons in the Kretschmann configuration for a Au-H_2O interface at 633 nm. The shaded area marked with 'TIR' (Total Internal Reflection) denotes the region below the critical angle (41.8°)

the x-direction at the interface between the metal and the dielectric medium located above; the evanescent field is confined in the z-direction, as also shown schematically in Fig. 2.1a. To excite the SPP wave, first an incident wave must match the polarization properties of the SPP and, therefore, a TM(p)-polarized wave is required (components E_x, H_y, E_z). Second, the incident wave must also match the tangential wavenumber of the SPP, k_{SPP}; this is provided by the substrate, as shown schematically in Fig. 2.1a and explained in Fig. 2.1b. There it is shown that the dispersion of the SPP lies below the lightline in the dielectric ($k_{\text{SPP}} > k_d$; k_d: wavenumber in the dielectric) and, hence, the incident wave must have a high tangential wavenumber k_{inc} to match k_{SPP} and achieve efficient power transfer to the SPP wave. This can be achieved, for example, via the incident angle θ in an angle-resolved experiment, as shown in Fig. 2.1c. For this example the wavelength of the incident wave is 633 nm, a typical wavelength employed in SPR spectroscopy, and the calculations have been performed for H_2O on a 50 nm Au layer and a prism of refractive index $n_{\text{sub}} = 1.5$ used as substrate. By expressing the tangential wavenumber of the incident wave as $k_{\text{inc}} = k_0 \cdot n_{\text{sub}} \cdot \sin\theta$, where k_0 is the free-space wavenumber, it becomes clear that k_{inc} can be controlled by both by θ and n_{sub}. Therefore, as θ is scanned, maximum power transfer from the incident wave to the SPP wave can be achieved at a certain angle where the condition $k_{\text{inc}} = k_{\text{SPP}}$ is met. At this angle, the excitation of the SPP wave becomes the most efficient and the reflected optical power is therefore minimized. This is manifested as a dip in the angle-resolved measured reflection.

The CHISPR sensing scheme is an extension of the typical SPR configuration, in which the dielectric layer is replaced by a chiral medium. Therefore, to understand the principles of CHISPR it is instructive first to examine the properties of SPPs at a metal-dielectric interface and how these are modified when the dielectric layer becomes chiral.

2.2.1 SPPs at a Metal-Dielectric Interface

The propagation characteristics of SPPs and their associated effects on the SPR have been widely discussed in many textbooks [41–43] and papers [42, 44–52]. To find the analytical form of the SPP, one starts with solving Maxwell's equations for the simple case of a flat interface between two semi-infinite spaces (conductor and dielectric), i.e. (2.2)–(2.5) with $\kappa = 0$. Although realistic systems do not involve semi-infinite material regions, the results are directly applicable to metallic films of finite thickness, because the field penetration inside the metallic region is usually much smaller than the thickness of the finite metallic layer (i.e., the film is is seen by the wave as having effectively infinite thickness).

Let us assume that the metallic layer extends along the xy-plane and SPP propagation occurs along the x-direction, with the evanescent field being confined in the z-direction, as shown schematically in Fig. 2.2. Both regions are non-magnetic ($\mu_r = 1$) and we may denote the relative permittivity ϵ_r of the metal and dielectric as ϵ_m and ϵ_d, respectively.

Due to the homogeneity of the geometry along the y-direction ($\partial/\partial y = 0$), Maxwell's equations are decomposed in two sets, one involving only H_x, E_y, H_z components (TE mode) and one involving only E_x, H_y, E_z components (TM mode). As also shown in [42], the SPP is a TM mode (it cannot exist for TE polarization) and, assuming propagation along the x-direction with propagation constant k_{SPP}, $H_y \sim e^{ik_{\mathrm{SPP}}x}$, ($\partial/\partial x = ik_{\mathrm{SPP}}$), the y-component satisfies the wave equation in both regions:

$$\frac{\partial^2 H_y}{\partial z^2} + (k_0^2 \epsilon_{m,d} - k_{\mathrm{SPP}}^2) H_y = 0, \tag{2.6}$$

where $\epsilon_{m,d}$ denotes ϵ_m or ϵ_d, depending on the material region this equation refers to. The solution for both sub-spaces is written in the form:

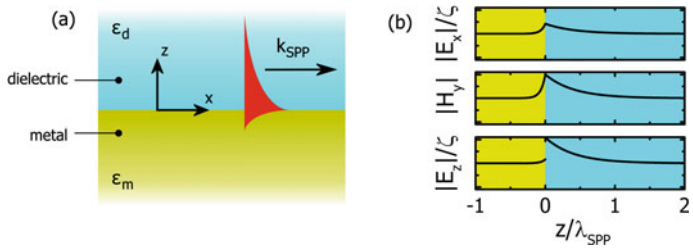

Fig. 2.2 Properties of SPPs at a metal-dielectric interface. **a** Geometry for SPP propagation **b** Field components of SPP wave at a Au-H_2O interface at 633 nm. The electric field components are normalized with ζ the wave impedance in H_2O and the penetration distance z is normalized with $\lambda_{\mathrm{SPP}} = 2\pi/\mathrm{Re}(k_{\mathrm{SPP}})$, the SPP wavelength. The SPP is studied analytically in the configuration shown in **a**, however the results are directly applicable to real SPR experiments with metallic films of finite size, as the field penetration inside the metal is usually much smaller than its thickness

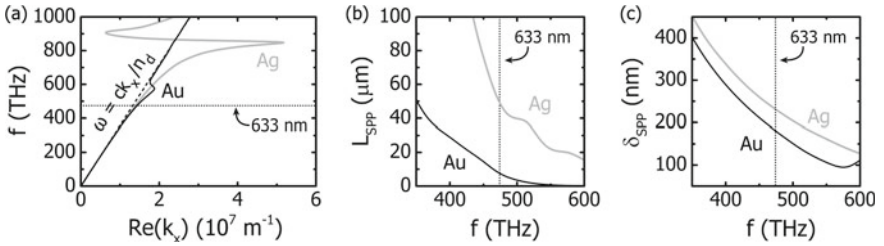

Fig. 2.3 SPP properties at a single interface between Ag-H_2O (grey lines) or Au-H_2O (black lines). **a** Dispersion relation. **b** Propagation length, L_{SPP}. **c** Penetration depth, δ_{SPP}. In all cases the dotted line marks the operation wavelength of 633 nm

$$H_y(z) = \begin{cases} H_0 e^{ik_{\mathrm{SPP}}x} e^{-k_d z}, & z \geq 0 \\ H_0 e^{ik_{\mathrm{SPP}}x} e^{+k_m z}, & z < 0 \end{cases}, \tag{2.7}$$

with

$$k_{m,d} = \sqrt{k_{\mathrm{SPP}}^2 - k_0^2 \epsilon_{m,d}}, \tag{2.8}$$

where H_0 is a complex constant common to both branches in (2.7)—satisfying the continuity of H_y at the interface—and $k_{m,d}$ is the wavenumber in the perpendicular direction that expresses the confinement in the metal (subscript 'm') or dielectric (subscript 'd') (the remaining E_x, E_z components are directly calculated from H_y using Maxwell's equations). The continuity of the tangential electric field, E_x, dictates that $k_d/k_m = -\epsilon_d/\epsilon_m$, which in combination with (2.8) leads to the dispersion relation of SPPs propagating at the interface between the two half-spaces:

$$k_{\mathrm{SPP}} = k_0 \sqrt{\frac{\epsilon_d \epsilon_m}{\epsilon_d + \epsilon_m}}. \tag{2.9}$$

This dispersion relation is associated with several important properties, see discussions in [44–46]. As an example, in Fig. 2.3a we plot (2.9) for a Ag-H_2O (grey line) and a Au-H_2O (black-line) interface (the material parameters for Ag and Au taken from [53], and for H_2O we use a constant $n_d = \sqrt{\epsilon_d} = 1.33$, the refractive index of water in the visible). The qualitative difference between the dispersion in Fig. 2.1b and both curves in Fig. 2.3a (i.e., the absence of a horizontal asymptote) is due to the high metallic losses of Ag and Au, which damp the propagating SPPs (see [45, 50, 54] for further details). The propagation distance of a SPP, L_{SPP}, is usually defined as the distance over which the mode can propagate along the supporting interface until the field amplitudes drop to $1/e$ of their initial magnitude, i.e. $L_{\mathrm{SPP}} = 1/\mathrm{Im}[\mathrm{k_{SPP}}]$ [50]. This is shown in Fig. 2.3b for the two cases considered here (L_{SPP} is typically between 10 and 100 μm in the visible regime, depending on the particular metal/dielectric material properties). In relevance to the SPR experiments that we are concerned here, the most important feature of (2.9) is that the dispersion branch related to the propagating SPP *(a)* lies below the lightline (i.e. the SPP is

confined to the interface) and *(b)* acquires high k-values with increasing frequency (i.e. the confinement becomes stronger); note that the SPP fields in the dielectric fall off as $e^{-|k_d||z|}$ with $k_d = \sqrt{k_{\mathrm{SPP}}^2 - k_0^2 \epsilon_d}$ [see (2.7), (2.8)]. The field-penetration depth $\delta_{\mathrm{SPP}} = 1/\mathrm{Im}[\mathrm{k_d}]$, i.e. the distance over which the field amplitudes drop to $1/e$ of their initial magnitude, is shown in Fig. 2.3c for both cases. As shown, δ_{SPP} is in the range of a few nm and, therefore, SPPs are ideal for sensing material changes particularly close to the metal-dielectric interface, such as those from thin-subwavelength in size-films.

2.2.2 SPPs at a Metal-Chiral Interface

The introduction of chirality in the dielectric medium that comprises the metal-dielectric system imposes changes in the features of the SPP, as examined in detail in the work of Mi and Van [51]. With chirality, SPPs are still supported at a metal-chiral interface, however both their field components and their dispersion change. Let us consider such an interface, where the chiral medium is characterized by permittivity ϵ_c, permeability μ_c, and chirality (Pasteur) parameter κ. Chirality introduces magneto-electric coupling by means of κ and, as a result, in the chiral medium the fields satisfy the coupled wave equations:

$$\nabla^2 \begin{bmatrix} \mathbf{E} \\ \mathbf{H} \end{bmatrix} + k_0^2 (n_c^2 + \kappa^2) \begin{bmatrix} \mathbf{E} \\ \mathbf{H} \end{bmatrix} + 2k_0 \kappa \begin{bmatrix} +i\omega\mu_c \mathbf{H} \\ -i\omega\epsilon_c \mathbf{E} \end{bmatrix} = \begin{bmatrix} 0 \\ 0 \end{bmatrix}, \tag{2.10}$$

where $n_c = \sqrt{\epsilon_c \mu_c}$ is the average (background) refractive index of the chiral medium. For propagation along the x-direction [$\mathbf{E}, \mathbf{H} \sim e^{ik_{\mathrm{SPP}}x}$ $(\partial/\partial x = ik_{\mathrm{SPP}})$] and homogeneity along the y-direction $(\partial/\partial y = 0)$, this system simplifies to:

$$\frac{\partial^2}{\partial z^2} \begin{bmatrix} \mathbf{E} \\ \mathbf{H} \end{bmatrix} + (k_0^2 (n_c^2 + \kappa^2) - k_{\mathrm{SPP}}^2) \begin{bmatrix} \mathbf{E} \\ \mathbf{H} \end{bmatrix} + 2k_0 \kappa \begin{bmatrix} +i\omega\mu_c \mathbf{H} \\ -i\omega\epsilon_c \mathbf{E} \end{bmatrix} = \begin{bmatrix} 0 \\ 0 \end{bmatrix}. \tag{2.11}$$

From the form of (2.11) it is evident that due to κ, each E-field component now couples with the respective H-field component and, therefore, all three components of the electric and magnetic field exist in both the metal and the chiral medium. The requirement for continuity of the tangential field components leads to the dispersion relation:

$$\left(\frac{\zeta_c k_{z,c+}}{k_{c+}} + \frac{\zeta_m k_{z,m}}{k_m} \right) \left(\frac{k_{z,c-}}{\zeta_c k_{c-}} + \frac{k_{z,m}}{\zeta_m k_m} \right) + \left(\frac{\zeta_c k_{z,c-}}{k_{c-}} + \frac{\zeta_m k_{z,m}}{k_m} \right) \left(\frac{k_{z,c+}}{\zeta_c k_{c+}} + \frac{k_{z,m}}{\zeta_m k_m} \right) = 0, \tag{2.12}$$

where $\zeta_c = \sqrt{\mu_c/\epsilon_c}$, $\zeta_m = \sqrt{\mu_m/\epsilon_m}$ is the wave impedance in the chiral medium and the metallic region, respectively and

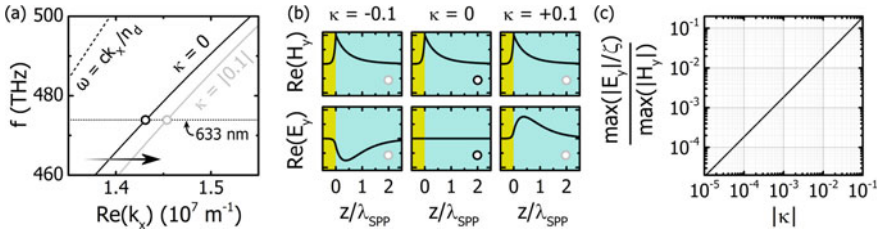

Fig. 2.4 Chiral SPP properties at a single Au-H_2O interface. **a** Dispersion relation for $\kappa = 0$ (black line) and $\kappa = \pm 0.1$ (grey line). Chirality shifts the dispersion to higher in-plane wavenumbers, independent of the sign of κ. This is also seen at the points marked with open circles, denoting operation at 633 nm. **b** Plots of H_y and E_y for $\kappa = -0.1$, $\kappa = 0$ and $\kappa = +0.1$. Chirality induces a non-vanishing E_y-component, with phase depending on the sign of κ. The open dots correspond to the dispersion points shown in **a**. **c** Magnitude of chiral-induced E_y-component in terms of $|\kappa|$, normalized with the magnitude of H_y-component (ζ: wave impedance in water)

$$k_{z,c\pm} = \sqrt{k_{\mathrm{SPP}}^2 - k_{c\pm}^2},\, k_{c\pm} = k_0 n_{\pm}, \tag{2.13}$$

$$k_{z,m} = \sqrt{k_{\mathrm{SPP}}^2 - k_m^2},\, k_m = k_0 n_m, \tag{2.14}$$

with $n_{\pm} = \sqrt{\epsilon_c \mu_c} \pm \kappa, n_m = \sqrt{\epsilon_m \mu_m}$ being the refractive index in the chiral medium and the metallic region, respectively.

This is the dispersion relation of SPPs propagating at a chiral-metal interface. Note that, in the limit $\kappa \to 0$, $k_{z,c+} \to k_{z,c-} \equiv k_{z,c}$, and the above relation reduces to the familiar dispersion of SPPs at an achiral dielectric-metal interface, which supports only the TM polarization (in this case ϵ_c is simply ϵ_d, as considered previously for the typical metal-dielectric interface). The chiral dispersion relation is also presented in the work of Mi and Van [51], however in a slightly different notation, due to the different formulation of the constitutive relations [52] (there, the chirality parameter is denoted as ξ and is related to κ as $\kappa = \zeta_0 \xi$, where ζ_0 is the vacuum wave impedance).

Using this dispersion relation, in Fig. 2.4 we examine the SPP properties at a single Au-H_2O interface, where a chiral medium is dispersed in the water region. To emphasize our findings, we assume a large chirality parameter ($\kappa \sim 0.1$). In Fig. 2.4a we present plots of the dispersion relation for $\kappa = 0$ (black line) and $\kappa = \pm 0.1$ (grey line), which demonstrate how chirality induces a shift to higher in-plane wavenumbers (k). This is also seen at the points marked with open circles, denoting operation at 633 nm; therefore, in an angle-resolved SPR experiment, chirality is expected to manifest as a shift of the reflectance dip at higher angles. Note that the k-shift does not depend on the sign of κ and, therefore, a typical SPR measurement cannot distinguish between left and right enantiomers. For the dispersion points marked with the open circles in Fig. 2.4a, in Fig. 2.4b we plot $\mathrm{Re}(H_y)$ and $\mathrm{Re}(E_y)$. We present individually three cases, namely for $\kappa = -0.1$, $\kappa = 0$ and $\kappa = +0.1$. From this plot it is evident that chirality modifies the pure-TM character of the SPP, thereby inducing a non-vanishing E_y-component. Most importantly, the phase of E_y depends on the sign of κ; as we will see in the next section, this is a key element

to our CHISPR protocol. Last, in Fig. 2.4c we plot the magnitude of E_y in terms of the magnitude of κ. To quantify the results with respect to the magnitude of H_y, we normalize E_y with the wave impedance ζ in water. The plot is shown in logarithmic scale, starting from realistic values of $|\kappa|(\sim 10^{-5})$ up to $|\kappa| = 0.1$, the value used in the examples of Fig. 2.4a, b. The linearity of this scaling is a second key element to our CHISPR protocol, as we will discuss in Sect. 2.3.

2.3 CHISPR

To demonstrate the principles of CHISPR we start by considering a standard angle-resolved SPR setup in the Kretschmann configuration [40] where a Au layer is deposited on a prism surface upon which a chiral substance dispersed in water is placed. A realistic rendering of such a setup is shown in Fig. 2.5.

To excite the SPP wave at the metal-chiral interface, a TM (p)-polarized wave is incident from the prism side (Figs. 2.1 and 2.5). For the case of a single metal-chiral interface we saw previously that the presence of the chiral layer qualitatively changes the SPP wave by generating an s-wave and by shifting the SPP dispersion to higher in-plane wavenumbers. Therefore, the properties of the chiral layer itself should be observable through angle-resolved SPR measurements; as discussed in the previous section, these are expected as an angular shift in the reflectance dip. In Fig. 2.6 we present the results of a simulated angle-resolved SPR experiment in the presence

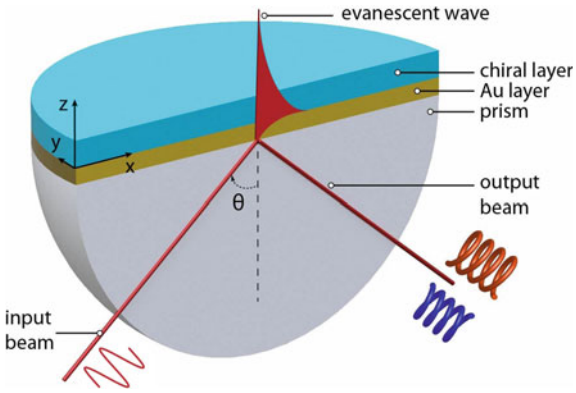

Fig. 2.5 CHISPR experimental setup (Kretschmann configuration) for the detection of chirality from thin (sub-wavelength) chiral layers: A linearly TM(p) polarized beam incident on a thin gold layer (Au layer thickness ~50 nm) excites a surface plasmon polariton (SPP) (indicated by the evanescent wave) at a particular angle, θ, which propagates along the metal-chiral interface. The SPP wave is modified by the chiral environment, resulting in an outgoing optical chirality flux which can be used to infer the properties of the chiral layer (see text for details). Figure reprinted with permission from [10]. Copyright 2020 American Chemical Society

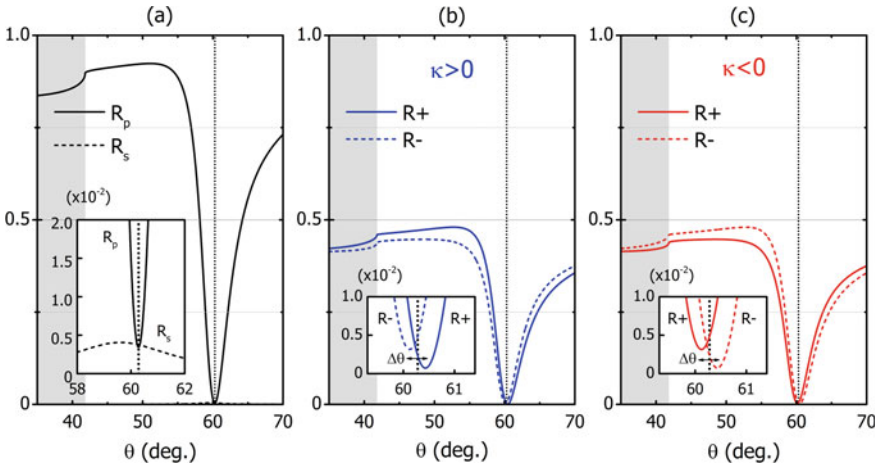

Fig. 2.6 SPR reflectance under the presence of a chiral layer ($n_c = 1.33$, 100 nm thickness). The SPR is excited with a TM(p)-polarized wave and the reflected power is analyzed into **a** p- and s-components, R_p, R_s, respectively (same for $\kappa = \pm 0.1$), and RCP (+) and LCP (-) components, R_+, R_-, respectively for **b** $\kappa = +0.1$ and **c** $\kappa = -0.1$. The effect of chirality appears in (a) as a enantio-independent angular shift of R_p, accompanied by nonzero R_s and in (b) & (c) as a chiral-dependent angular split ($\Delta\theta = \theta_+ - \theta_-$) between R_+ and R_-. The magnitude and sign of $\Delta\theta$ depends on $|\kappa|$ and sgn(κ), respectively. In all subplots, the vertical dashed lines denote the angle of minimum R_p, i.e. the SPR angle, and the shaded areas denote the region below the critical angle (41.8 deg)

of a thin chiral layer, where, to clarify our findings, we again use a large chirality parameter κ and consider both possibilities for the sign, i.e. $\kappa = \pm 0.1$.

We analyze the reflected wave in terms of s and p components and calculate the power at each polarization, namely R_s, R_p. Additionally, we analyze the total reflected power $R_s + R_p$ in terms of $+/-$ components, which we denote as $R_\pm = |r_\pm|^2$, where $r_+ (r_-)$ is the complex amplitude of the RCP (LCP) wave (that is, $R_+ + R_- = R_s + R_p$). In an actual experiment, measurement of $R_{s/p}$ and $R_{+/-}$ can be easily performed with the incorporation of a Stokes polarimeter at the analysis stage.

In Fig. 2.6a we show the reflected power measured in terms of s/p waves, as is typically performed and presented in SPR experiments. The R_p curve has a pronounced reflection-dip at 60.3 deg, indicating the excitation of a SPP wave, while we also observe a nonzero R_s peaking at 59.5 deg [Fig. 2.6a, inset], as now part of the p-wave is transferred to the s-wave due to the presence of the chiral layer. We note here that, in accord with our analysis in Sect. 2.2.2, κ induces a shift on R_p towards larger angles and this shift is identical for both $\kappa = \pm 0.1$ [for $\kappa = 0$, the R_p reflection-dip is located at 60.1 deg, while $R_s = 0$, as also shown in Fig. 2.1c]. Thus, *measurement analysis based on the s/p waves cannot differentiate between left-handed and right-handed chiral substances*. We also note that this measurement modality has been used in previous works discussing the possibility of detecting

chirality using SPR measurements [55, 56], but it is effectively insensitive to the sign of the chiral parameter κ.

When we now analyze the reflected wave in terms of RCP/LCP $(+/-)$ components, we observe that the minima of the R_+, R_- reflectances do not coincide, but are separated by an angle $\Delta\theta \equiv \theta_+ - \theta_-$, where θ_+ (θ_-) denotes the angle of the R_+ (R_-) minimum [Fig. 2.6b, c]. Moreover, we observe that for $\kappa > 0$ $(\kappa < 0)$, $\Delta\theta > 0$ $(\Delta\theta < 0)$. Thus, the presence of a thin chiral layer results in a *chiral-dependent angular split* $\Delta\theta$ between the measured reflectances of R_+ and R_-, which has a distinct behaviour depending on the sign and magnitude of κ. We wish to note here that our polarimetric measurement scheme, where the reflected wave is analyzed in terms of $+/-$ components, is sensitive only to chiral effects and not to general spectral shifts (possible if variations to the host refractive index are present), and moreover it is equivalent to the chirality flux spectroscopy used to probe the chiral near-fields of chiral nanosystems, as presented in [57].

2.3.1 Mechanism of Chiral-Dependent SPR-Reflectance Angular Split

To understand the mechanism behind the chiral-dependent SPR-reflectance angular split, we examine how the near-field properties of the SPP wave are associated with the properties of the reflected wave in the far-field. We start by analyzing the SPP wave along its propagation direction (x) into $+/-$ components, i.e. $\mathbf{A}_{\mathrm{SPP}} = A_y\hat{y} + A_z\hat{z} = A^{+}_{\mathrm{SPP}}(\hat{y} + i\hat{z}) + A^{-}_{\mathrm{SPP}}(\hat{y} - i\hat{z})$, where $A^{\pm}_{\mathrm{SPP}} = (A_y \mp A_z)/2$ and $\mathbf{A}$ is any of the electromagnetic field quantities $\mathbf{E}$, $\mathbf{H}$, $\mathbf{B}$, $\mathbf{D}$; then, we calculate the electric and magnetic energy densities $w_e^{\pm} = (1/4)\mathbf{E}^{\pm}_{\mathrm{SPP}}(\mathbf{D}^{\pm}_{\mathrm{SPP}})^*$ and $w_m^{\pm} = (1/4)\mathbf{B}^{\pm}_{\mathrm{SPP}}(\mathbf{H}^{\pm}_{\mathrm{SPP}})^*$, respectively, which we integrate to find the total energy stored in each of the two $(+/-)$ components, namely $W_{\pm} = \int_{\mathrm{V}}(w_e^{\pm} + w_m^{\pm})\,\mathrm{d}^3x$ [Fig. 2.7a]. Here, the integration volume V is the entire SPP volume extending above the metal (where the chiral layer is to be probed). For $\kappa = 0$ we obtain $W_+ = W_-$, as the SPP wave has only an E_z-component on the yz-plane, which is equally distributed between the two $+/-$ components (typical nonchiral SPR case). This is shown in Fig. 2.7b, where the energy difference $W_+ - W_-$ is normalized to the incident energy $S_{\mathrm{inc}}/2\omega$ (ω is the angular frequency and S_{inc} is the magnitude of the time-averaged Poynting vector). However, the onset of chirality causes the emergence of an E_y-component [51] and, hence, an unbalanced storage of the optical energy between the $+/-$ components of the SPP. In fact, for $\kappa > 0$ $(\kappa < 0)$, RCP (LCP) components are favoured and, therefore, $W_+ > W_-$ $(W_+ < W_-)$ [Fig. 2.7b]. This stored energy excess between $+/-$ SPP components in the near-field results in nonzero R_s reflectance in the far-field; this is apparent in the fact that the peak of R_s coincides with the peak of $W_+ - W_-$ at 59.5 deg which differs from the R_p minimum at 60.3 deg [Figs. 2.6a and 2.7b]. In other words, the E_y-component that emerges in the near-field due to chirality, is identified in the far-field as well, as power transfer from the outgoing p-wave

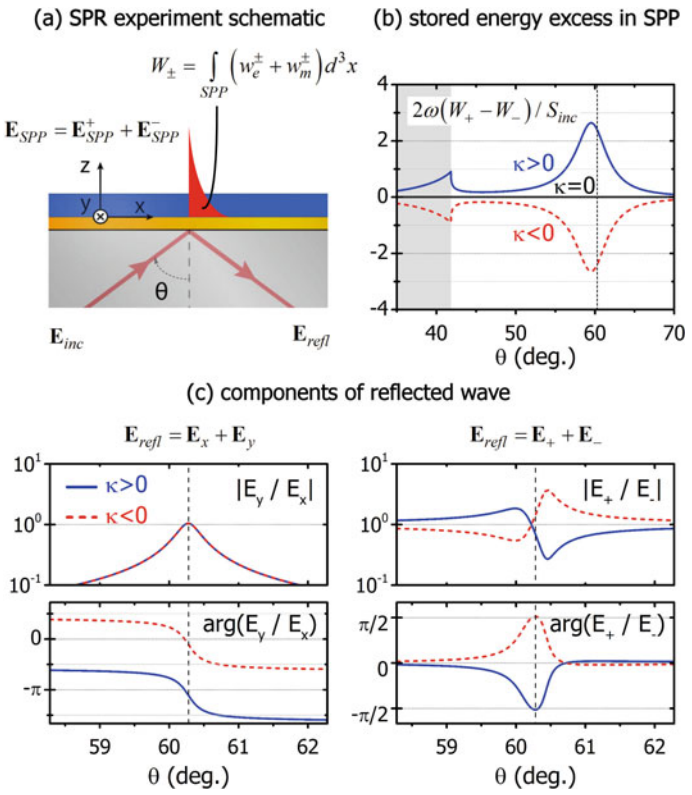

Fig. 2.7 Mechanism of the R_+, R_- angular split. **a** The incident wave excites the SPP, which we analyze in RCP/LCP $(+/-)$ components along its propagation direction. The total energy stored in each component is denoted as $W_\pm$ (see also text for details). **b** Stored energy difference between RCP/LCP components of the SPP wave (normalized over the incident energy $S_{\text{inc}}/2\omega$). Chirality causes energy excess between RCP/LCP waves, which changes sign upon sign change of κ ($\kappa = \pm 0.1$). **c** Ratio of amplitude and phase of the reflected wave components for $\kappa = +0.1$ (solid blue lines), $\kappa = -0.1$ (dashed red lines). We analyze the wave in terms of s/p components (left) and RCP/LCP components (right). We present the amplitude in logarithmic scale to emphasize the inversion symmetry of the ratio $|E_+/E_-|$ upon sign change in κ. The vertical dashed line denotes the angle of minimum R_p, i.e. the SPR angle. Figure adapted with permission from [10]. Copyright 2020 American Chemical Society

to the s-wave. When the total reflected wave in the far-field is analyzed in $+/-$ components as well, the reflectance splits into two parts, which have their minima at different angles [Fig. 2.6b, c]. This angular split is mediated by the resonance of the surface plasmon; the amplitude of the E_y/E_x ratio is symmetric around the SPR angle [Fig. 2.7c], however, the phase $\arg(E_y/E_x)$ undergoes a π-shift, favouring the advance of either the E_x or the E_y component, depending on whether the angle of incidence is below or above the SPR angle [Fig. 2.7c]. Consequently, the mixture of the reflected RCP and LCP wave-components is weighted differently, resulting in

an excess of either RCP or LCP waves below or above the SPR angle and, hence, a reflectance split between R_+ and R_- waves. As for the magnitude of κ, it does not significantly affect the $\arg(E_y/E_x)$ (it induces a slight angular shift), however, it notably changes the amplitude of E_y/E_x, which increases with increasing κ. Changing the sign of κ induces a π-shift of the E_y phase, without affecting E_x [Fig. 2.7c]. Hence, the sign of κ does not affect the amplitude of the ratio E_y/E_x but causes the interchange between RCP/LCP components.

2.3.2 *Sensitivity of Chiral-Dependent SPR-reflectance Angular Split*

Because the resonance of the SPP wave depends strongly on the material parameters at the metal-chiral interface, it is expected that the strength of the SPR reflectance angular split $\Delta\theta$ will depend, besides the chirality parameter κ, also on the chiral substance's refractive index, n_c.

In Fig. 2.8 we show this dependence for the case of real κ (we discuss the case of imaginary κ in a following section). Overall, we observe *(a)* a linear dependence between the magnitudes of $\Delta\theta$ and κ, *(b)* a distinct correspondence between the signs of $\Delta\theta$ and κ, and *(c)* a non-monotonic dependence of $\Delta\theta$ on n_c. This non-monotonic dependence is related to the interplay between the coupling strength of the incident wave to the SPP wave and the interaction strength of the SPP wave with the chiral layer. In particular, as n_c increases, the SPR dispersion changes and the reflection-dip is shifted to higher angles due to higher k_{SPP} [Fig. 2.8a]. In turn, the coupling of the incident wave to the SPP becomes stronger, leading to higher $\Delta\theta$ and, hence, in increased sensitivity [Fig. 2.8b]. Eventually, for very high incident angles the coupling of the incident wave to the SPP becomes weaker, leading to weaker $\Delta\theta/\Delta\kappa$ accordingly. In addition, for angles close to the critical angle the effect becomes the weakest. In reflection-based polarimetric measurements, the optical rotation signals scale as $\sim\sqrt{\mathrm{Re}(\kappa)}$ when approaching the critical angle (see [23, 24, 58, 59]), which is not the case here [Fig. 2.8b]. This is a consequence of the fact that the measurement is mediated entirely by the SPP wave and is not associated with direct polarimetric signals from the chiral layer. Thus, by measuring the magnitude and sign of this chiral-dependent angular split, we obtain information about the magnitude and sign of κ.

Furthermore, because the thickness of the chiral film is finite, the SPP interacts both with the chiral film and the dielectric region above (air). In essence, the SPP experiences an effective index in the chiral-air region, which depends on the chiral film thickness; with increasing film thickness, the evanescent tails of the SPP interact less and less with the air above, until this effective index converges to n_c. In our simulations so far we considered a chiral layer of 100 nm thickness, which is in the order of the calculated field penetration depth [see Fig. 2.3b]. For this reason, in Fig. 2.9 we repeat the calculations of the measurement sensitivity ($\Delta\theta/\Delta\kappa$) pre-

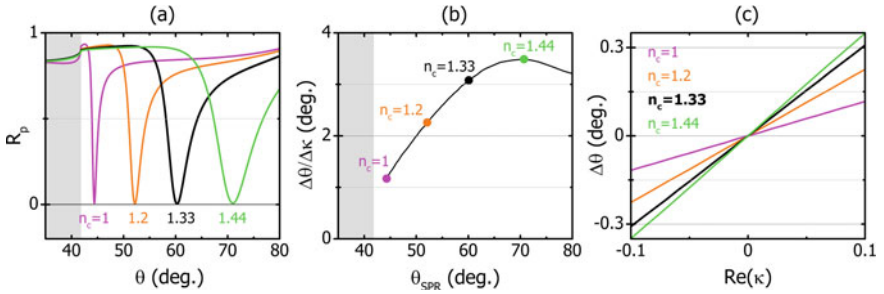

Fig. 2.8 Measurement sensitivity of $\Delta\theta$ on the chirality parameter κ. **a** Angle-resolved R_p reflectance denoting the SPR angle (θ_{SPR}) for the shown selected values of n_c with $\kappa = 0$. **b** $\Delta\theta/\Delta\kappa$ vs SPR angle. The solid black line represents a multitude of individual calculations, on which the cases for n_c shown in (a) are marked with dots of the same colour. **c** $\Delta\theta$ vs κ for the selected values of the host index n_c. The solid black line denotes the system of Fig. 2.6 with $n_c = 1.33$

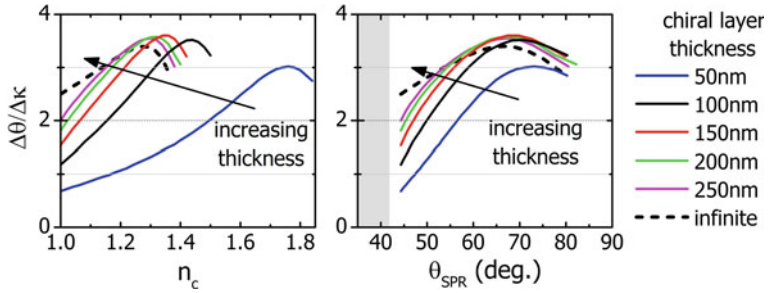

Fig. 2.9 $\Delta\theta/\Delta\kappa$ as a function of the chiral-layer thickness, for $\kappa = 0.1$. The dashed black line represents the results shown in Fig. 2.8

sented in Fig. 2.8b, for chiral layers of variable thickness. We see that, with increasing chiral layer thickness, the measurement sensitivity converges to the limit of chiral substances of theoretically infinite extent (practically referring to electrically thick samples). In addition, we observe that for small SPR angles this increase is monotonic, but for large SPR angles the measurement sensitivity reaches a maximum level for a thickness of ∼100–150 nm, beyond which it gradually drops until convergence. Therefore, we see that due to the evanescent character of the SPP wave inside the chiral region, one can achieve through measurements of $\Delta\theta$ similar levels of sensitivity for a large range of chiral-layer thicknesses.

2.3.3 *Differential Measurements*

In the previous subsections we demonstrate how the presence of a thin chiral layer results in a *chiral-dependent angular split* between the measured reflectances of R_+

and R_-, which has a distinct behaviour depending on the sign and magnitude of κ. However, as we show in Fig. 2.8, for small values of κ ($\kappa < 10^{-3}$), this angular split, $\Delta\theta$, becomes similarly small and its detection can be hindered by background noise sources. Despite this, there exist alternative measurements one can consider performing in a CHISPR scheme, thanks to the ability to obtain distinct chiral-dependent signals. In particular, we can consider measurement configurations based on differential signals which are largely immune to signal fluctuations and drifts (a direct analogy is the case of CD measurements, which are differential type of measurements). Specifically, we consider two relevant quantities associated with the reflected (outgoing) RCP/LCP waves: the amplitude and phase differential reflectances (DR), namely ρ_{DR} and ϕ_{DR}, respectively. We define the DR signals as,

$$\rho_{\mathrm{DR}} = \frac{|r_+|^2 - |r_-|^2}{|r_+|^2 + |r_-|^2}, \text{ and } \phi_{\mathrm{DR}} = \mathrm{Arg}\left[\frac{\mathrm{r}_+}{\mathrm{r}_-}\right]. \tag{2.15}$$

In Fig. 2.10 we present the DR signals, ρ_{DR} and ϕ_{DR}, respectively, for a value of $\kappa = \pm 10^{-5}$ as a function of the background index of the chiral layer, n_c. We

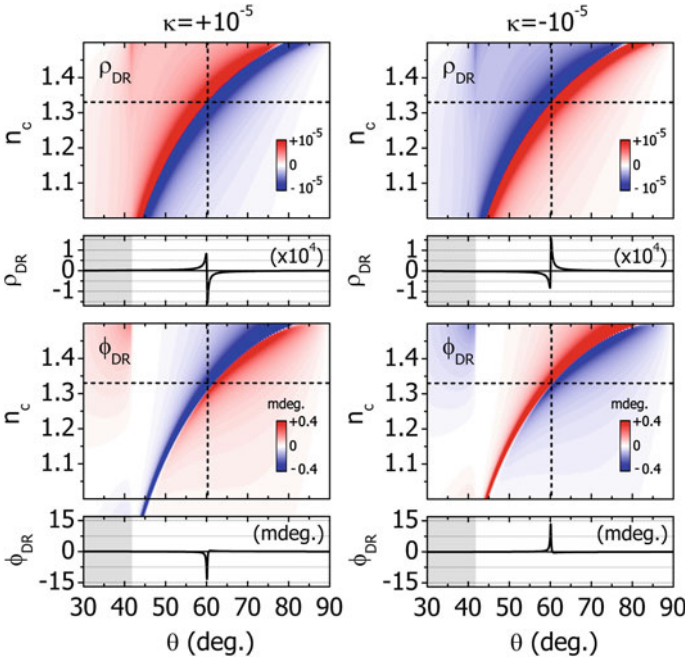

Fig. 2.10 Differential reflectance (DR) signals for a 100 nm thin chiral layer with $\kappa = \pm 10^{-5}$, as a function of the background index of the chiral layer (n_c). The shown range is $\sim(-6.3 \ldots + 6.3) \times 10^{-2} \times \max(\rho_{\mathrm{DR}})$ in the ρ_{DR} plots and $\sim(-2.7 \ldots + 2.7) \times 10^{-2} \times \max(\phi_{\mathrm{DR}})$ in the ϕ_{DR} plots to emphasize the broadening with increasing SPR angle and the distinct association with the sign of κ. Specific examples for $n_c = 1.33$ are marked with horizontal dashed lines and are shown separately below each panel. The vertical dashed line marks the SPR angle for the chosen value of n_c

emphasize here that this is a realistic value for the chirality parameter, corresponding, for example, to the case of aqueous solutions of monosaccharides [23, 24] or biomolecules [34–36]. For such a realistic value of κ, therefore, we observe ρ_{DR} signals of the order of $\sim 10^{-4}$ and ϕ_{DR} signals of the order of a few $\sim$mdegs, both within the sensitivity range of SPR instruments [60–62]. As a comparison, we note that the optical rotation signal from a transmission measurement of a 100 nm chiral layer with $\kappa = +10^{-5}$ at 633 nm, is $\varphi \simeq 6 \times 10^{-4}$ deg (2.1). Furthermore, we observe that $\rho_{\mathrm{DR}}(-\kappa) = -\rho_{\mathrm{DR}}(\kappa)$ and $\phi_{\mathrm{DR}}(-\kappa) = -\phi_{\mathrm{DR}}(\kappa)$. Thus, using the DR-dependent signals, we are able to quantify $\mathrm{Re}(\kappa)$ (magnitude and sign) with increased sensitivity compared to measurements of the angular split, $\Delta\theta$ [61, 63, 64].

Another important feature of the differential signals, ρ_{DR} and ϕ_{DR}, is that these decrease in amplitude as the plasmon resonance moves away from the critical angle, contrary to $\Delta\theta/\Delta\kappa$ which we observe to increase (Fig. 2.8). This decrease is related to the broadening of the SPR feature due to increased losses for higher k_{SPP}, and to the reduction of the R_s/R_p ratio, which expresses the strength of the p- to s-wave conversion. In particular, in Fig. 2.11 we show the change in the R_s/R_p ratio with increasing SPR angle (due to increasing n_c). We observe that the R_s/R_p ratio decreases while simultaneously broadening, which yields, thus, reduced differential signals. Moreover, the peak-to-peak values of ρ_{DR} and ϕ_{DR} [$\Delta\rho_{\mathrm{DR}}$ and $\Delta\phi_{\mathrm{DR}}$, respectively; Fig. 2.11b], qualitatively follow a similar trend indicating a strong connection with the strength of R_s/R_p. Furthermore, we observe that the variation of R_s/R_p (and consequently of $\Delta\rho_{\mathrm{DR}}$ and $\Delta\phi_{\mathrm{DR}}$) is non-monotonic and it generally depends on the properties of the particular metal. Despite these, it is apparent that regardless of the exact variation, the differential signals of ρ_{DR} and ϕ_{DR} allow for unambiguous determination of κ.

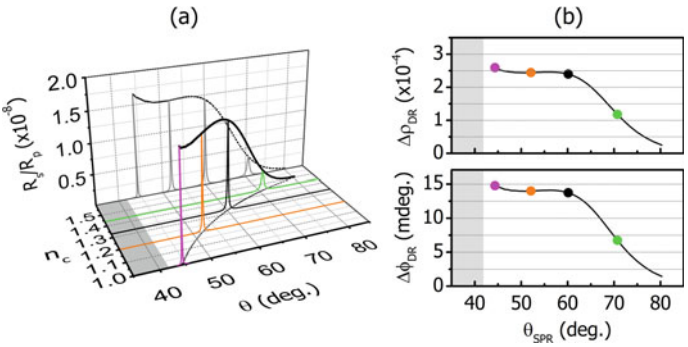

Fig. 2.11 Effect of coupling strength between $s-$ and $p-$waves due to chirality on differential reflection measurements. **a** R_s/R_p ratio as function of n_c for $\kappa = \pm 10^{-5}$. **b** Peak-to-peak values of the differential signals ρ_{DR} and ϕ_{DR} [$\Delta\rho_{\mathrm{DR}}$ (top) and $\Delta\phi_{\mathrm{DR}}$ (bottom), respectively]. The solid black lines represent a multitude of individual calculations, on which the cases for n_c shown in **a** are marked with dots of the same colour. In addition, the marked cases in **a**, **b** correspond to the cases shown in Fig. 2.8 using the same colour-code

2.4 Complete Measurement of Chirality

So far we have examined CHISPR signals assuming only a real-valued chirality parameter κ. Under realistic experimental conditions, this is a valid approximation for interpreting the results when one performs measurements at optical frequencies far detuned from any molecular resonances where chiral-dependent differential absorption (i.e. circular dichroism), which is proportional to $\mathrm{Im}(\kappa)$, is negligible [11]. However, when the optical frequency of an SPR instrument is near a molecular transition, both circular birefringence and circular dichroism [proportional to $\mathrm{Re}(\kappa)$ and $\mathrm{Im}(\kappa)$, respectively] become substantial and the proposed measurements should be interpreted with care.

To examine circular dichroism effects we introduce a nonzero imaginary part in the chirality parameter κ and demonstrate its effect on the CHISPR signals. However, to appropriately examine the case of circular dichroism (by introducing an imaginary part in the chirality parameter κ) without violating the passivity, we must ensure that $\mathrm{Im}(n_c \pm \kappa) > 0$. For this reason, we introduce artificial loss in the average refractive index of the chiral layer, i.e. $n_c = 1.33 + 0.01\,i$.

We start by demonstrating how each CHISPR signal ($\Delta\theta$ and DR signals) change under the influence of an imaginary-valued chirality parameter. In Fig. 2.12a we present the chiral-dependent angular split $\Delta\theta$ as a function of $\mathrm{Re}(\kappa)$ for $\mathrm{Im}(\kappa) = -10^{-3}, 0, 10^{-3}$. We see that in the presence of absorption [$\mathrm{Im}(\kappa) \neq 0$] the angular split $\Delta\theta$ obtains a *linear chiral-dependent offset*, and the effects of $\mathrm{Re}(\kappa)$ and $\mathrm{Im}(\kappa)$ appear as linear superpositions in the total $\Delta\theta$. Moreover, in Fig. 2.12b we present the change in the differential signals, ρ_{DR} and ϕ_{DR}, in the presence of absorption. In particular, we calculate ρ_{DR} and ϕ_{DR} for $\kappa = 10^{-5}$, $\kappa = 10^{-5}\,i$, and the sum of the two individual signals. We also present the same signals for the case of $\kappa = 10^{-5} + 10^{-5}\,i$, which we show to coincide with the sums of the individual signals [Fig. 2.12b]. In overall, we see that in the presence of absorption and birefringence, the effects of the real and imaginary parts of the chirality parameter appear as linear superpositions in the final CHISPR signals ($\Delta\theta$ and DR signals).

In Fig. 2.13 we examine the resulting DR signals for the cases of both chiral-dependent refraction, $\kappa = \pm 10^{-5}$, and absorption, $\kappa = \pm 10^{-5}\,i$. From the individual simulations we observe a clear distinction in the DR signals between the four cases, that is, CHISPR enables the detection of the magnitude and sign of both the real and imaginary part of the chirality parameter, and discrimination of their contribution through the distinct CHISPR signals. In combination with the results shown in Fig. 2.12, it becomes apparent that in the case where the SPR operational wavelength is near the vicinity of a molecular resonance, where circular dichroism is accompanied by an dispersive circular birefringence, i.e $\mathrm{Re}(\kappa)$ & $\mathrm{Im}(\kappa) \neq 0$ (Cotton effect [11]), the resulting DR signals will be the result of a linear superposition of the individual signals for the real and the imaginary part of the total chirality parameter (as these are presented in Fig. 2.13).

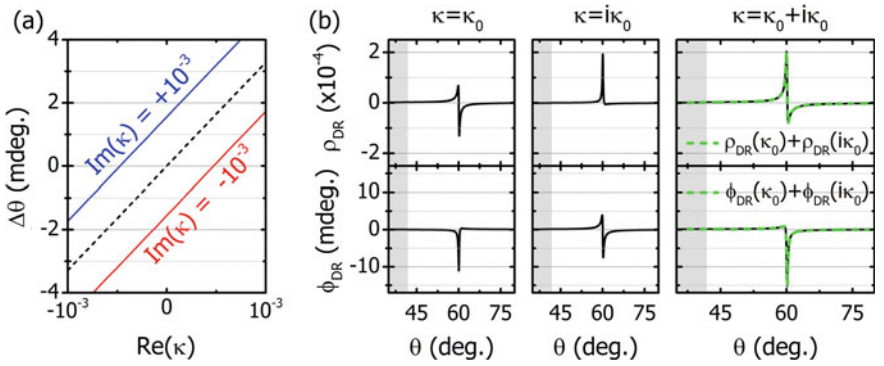

Fig. 2.12 CHISPR measurements in the presence of molecular absorption, i.e. $\mathrm{Im}(\kappa) \neq 0$. **a** $\Delta\theta$ as a function of $\mathrm{Re}(\kappa)$ for $\mathrm{Im}(\kappa) = \pm 0.001i$ [dashed line corresponds to $\mathrm{Im}(\kappa) = 0$]. To maintain the passivity of the system, we add artificial loss to the chiral layer index, which now is $n_c = 1.33 + 0.01i$.**b** Demonstration of linearity of the effects of $\mathrm{Re}(\kappa)$ and $\mathrm{Im}(\kappa)$ on the differential signals ρ_{DR} and ϕ_{DR}. The calculations have been performed for $\kappa = \kappa_0$ (left) and $\kappa = i\,\kappa_0$ (middle) separately, and for $\kappa = \kappa_0 + i\,\kappa_0$ (right), with $\kappa_0 = 10^{-5}$. Here we use: $n_c = 1.33 + 10^{-3}i$. Figure adapted with permission from [10]. Copyright 2020 American Chemical Society

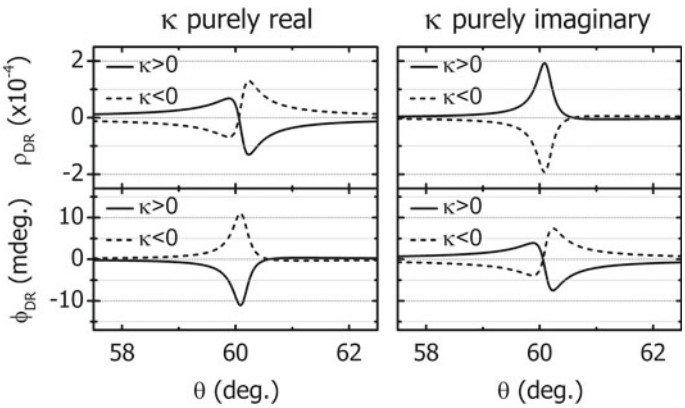

Fig. 2.13 Complete sensing of total chirality via measurements of the differential signals ρ_{DR} and ϕ_{DR}. *Left column*: $\kappa = \pm 10^{-5}$ (purely real). *Right column*: $\kappa = \pm 10^{-5}i$ (purely imaginary). Here we use: $n_c = 1.33 + 10^{-3}i$

2.5 Optical Chirality Conservation

The fact that the presence of the chiral layer modifies the evanescent field of the SPP, naturally raises the question of whether the reflectance measurements in the far-field can provide information about the chiral near-field features. To relate the two quantities, we utilize the conservation law of optical chirality density [65–70], which in the time-averaged, time-harmonic case is written as:

$$-2\omega \int_{\mathrm{V}} \mathrm{Im}(\chi_e - \chi_m)\,\mathrm{d}^3x + \int_{\mathrm{V}} \mathrm{Re}(\nabla \cdot \mathbf{F})\,\mathrm{d}^3x = 0, \tag{2.16}$$

where χ_e and χ_m are the electric and magnetic optical chirality densities, respectively, and $\mathbf{F}$ is the corresponding chirality flux:

$$\chi_e = \frac{1}{8}\Big[\mathbf{D}^* \cdot (\nabla \times \mathbf{E}) + \mathbf{E} \cdot (\nabla \times \mathbf{D}^*)\Big], \tag{2.17}$$

$$\chi_m = \frac{1}{8}\Big[\mathbf{H}^* \cdot (\nabla \times \mathbf{B}) + \mathbf{B} \cdot (\nabla \times \mathbf{H}^*)\Big], \tag{2.18}$$

$$\mathbf{F} = \frac{1}{4}\Big[\mathbf{E} \times (\nabla \times \mathbf{H}^*) - \mathbf{H}^* \times (\nabla \times \mathbf{E})\Big]. \tag{2.19}$$

Similarly to as we performed in Sect. 2.3.1, here we again analyze the SPP wave along its propagation direction (x) into $+/-$ components. For $\kappa \neq 0$ the integral of the total chirality density $\chi = \chi_e + \chi_m$ across the SPP volume, X, is unequally stored between the $+/-$ SPP components, i.e. $|X_+| \neq |X_-|$, where $X_\pm = \int_{\mathrm{V}} (\chi_e^\pm + \chi_m^\pm)\,\mathrm{d}^3x$. Because X_+ and X_- are associated with waves of the opposite handedness, they possess opposite sign and, hence, the total X, which is the sum $X_+ + X_-$, is written as $|X_+| - |X_-|$, which expresses a chirality excess between the $+/-$ components. In Fig. 2.14 we plot the integrated optical-chirality-density excess $|X_+| - |X_-|$, and to directly relate it with the simulations we present in Fig. 2.6 we choose $\kappa = 0,\ \pm 0.1$. We see that the result is qualitatively similar to $W_+ - W_-$, as shown in Fig. 2.7b. Due to the chirality conservation law (2.16), this unbalance results in a chirality flux $\mathbf{F}$ in the far-field, manifested as unequal RCP and LCP components and observed through the angular split or the DR signals. In fact, as shown in [70] the chirality flux $\mathbf{F}$ of a certain propagating wave is proportional to the third Stokes parameter, and also related to the Poynting vector $\mathbf{S} = \frac{1}{2}(\mathbf{E} \times \mathbf{H}^*)$, via $F_\pm = \mp(\omega/c)S_\pm$ (where c is the speed of light in the medium, and $F_\pm$ and $S_\pm$ are the magnitudes of $\mathbf{F}$ and $\mathbf{S}$ with the signs $+/-$ corresponding to RCP/LCP waves, respectively). Therefore, in the CHISPR measurement protocol, there must be a connection between the measurable reflectances R_+, R_- and the far-field chiral quantities.

To find this connection, we start by analyzing the incident wave in $+/-$ components. We calculate the magnitudes of the power flux $S_{\mathrm{inc}}^\pm$ and chiral flux $F_{\mathrm{inc}}^\pm$ for each component and, because the incident wave is linearly polarized (p-wave), we find that these quantities are equally distributed between the $+/-$ components, i.e. $S_{\mathrm{inc}}^+ = S_{\mathrm{inc}}^- \equiv S_{\mathrm{inc}}/2$ and $F_{\mathrm{inc}}^+ = F_{\mathrm{inc}}^- \equiv F_{\mathrm{inc}}/2$, where S_{inc} and F_{inc} are the magnitudes of the total incident power and chiral flux, respectively. In fact, because the incident wave is linearly polarized, the total incident chirality flux is zero, i.e. $\mathbf{F}_{\mathrm{inc}} = \mathbf{F}_{\mathrm{inc}}^+ + \mathbf{F}_{\mathrm{inc}}^- = 0$. However, because the individual fluxes have nonzero magnitude (and equal; they correspond to circularly polarized waves of equal amplitude), we define the incident flux magnitude as $F_{\mathrm{inc}} = |\mathbf{F}_{\mathrm{inc}}^+| + |\mathbf{F}_{\mathrm{inc}}^-| = 2|\mathbf{F}_{\mathrm{inc}}^\pm| \equiv 2F_{\mathrm{inc}}^\pm$.

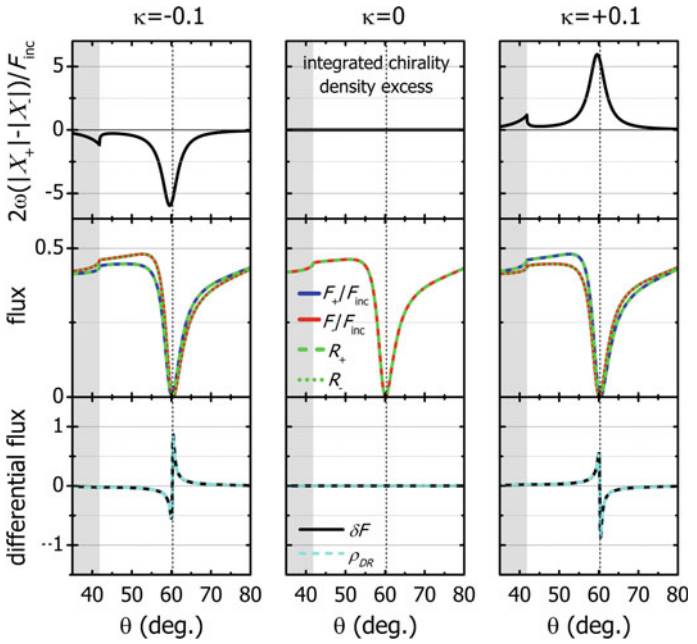

Fig. 2.14 Top row: Integrated optical chirality density excess $X_+ - X_-$ between RCP/LCP $(+/-)$ components of the SPP wave, normalized with the incident $F_{\text{inc}}/2\omega$. Middle row: Reflected chirality flux $F_\pm$ (solid blue/red lines), normalized with the incident chirality flux F_{inc}, and reflectance $R_\pm$ (dashed/dotted lines). Bottom row: differential flux δF and differential reflectance amplitude ρ_{DR}. For these simulations we use a 100 nm thin chiral layer with $n_c = 1.33$ and $\kappa = -0.1$ (left column), $\kappa = 0$ (middle column) and $\kappa = +0.1$ (right column). In all panels, the SPR angle (angle of minimum R_p) is marked with a vertical dashed line. Figure adapted with permission from [10]. Copyright 2020 American Chemical Society

Next, after following a similar analysis for the reflected wave, we associate the quantities related to both the incident and reflected $+/-$ components as,

$$F^{\pm}_{\text{inc}} = \mp\frac{\omega}{c} S^{\pm}_{\text{inc}}, \quad F^{\pm}_{\text{refl}} = \mp\frac{\omega}{c} S^{\pm}_{\text{refl}}, \tag{2.20}$$

and hence

$$\frac{F^{\pm}_{\text{refl}}}{F^{\pm}_{\text{inc}}} = \frac{S^{\pm}_{\text{refl}}}{S^{\pm}_{\text{inc}}} \Rightarrow \frac{F^{\pm}_{\text{refl}}}{F_{\text{inc}}} = \frac{S^{\pm}_{\text{refl}}}{S_{\text{inc}}} \equiv R_\pm, \tag{2.21}$$

or simply $F_\pm/F_{\text{inc}} = R_\pm$. As a result, we find that the reflected chirality flux $F_\pm$, normalized by the incident optical chirality flux F_{inc}, is equal to the reflectance $R_\pm$ in the CHISPR measurement protocol. To emphasize this equivalence, in Fig. 2.14 we present calculations of $F_\pm/F_{\text{inc}}$ and $R_\pm$ for the three cases considered, namely $\kappa = 0, \kappa = \pm 0.1$. Therefore, we see that our proposed measurement scheme results in a direct measurement of the optical chirality flux, which is directly connected with

the near-field optical chirality density [65–70]. Moreover, using $F_{\pm}/F_{\text{inc}} = R_{\pm}$ it follows that:

$$\delta F = \frac{F_+ - F_-}{F_+ + F_-} = \frac{R_+ F_{\text{inc}} - R_- F_{\text{inc}}}{R_+ F_{\text{inc}} + R_- F_{\text{inc}}} = \frac{R_+ - R_-}{R_+ + R_-} = \rho_{\text{DR}}, \tag{2.22}$$

i.e. the differential chirality flux δF is equal to ρ_{DR}, as we also demonstrate in Fig. 2.14.

2.6 Discussion and Conclusions

In this chapter, we start from the observation that plasmonic near fields at metal-chiral interfaces exhibit non-vanishing optical chirality density, which generates a far-field chirality flow. By measuring this chirality flow, which we show to be simply the reflectance in our measurement protocol, we are able to detect changes in the near-field chirality and we demonstrate how this can be exploited for chiral-sensitive measurements using SPR instrumentations. From this, we proceed to demonstrate the following: *(a)* how chiral-sensitive SPR measurements allow for the complete determination of chirality of a natural optically active substance (handedness and magnitude) and for the detection of the near-field wave at the metal-chiral interface; *(b)* how CHISPR is able to detect both the real and imaginary part of the chiral index of refraction, i.e. detect both circular birefringent and circular dichroism effects; and *(c)* how CHISPR is particularly sensitive for the case of sub-wavelength chiral layers, for which traditional (commercial) polarimetry has typically insufficient sensitivities to detect. A particularly significant advantage of the angle-resolved CHISPR protocol we present here, is that it can be employed for spectroscopy of a molecule simply by tuning the frequency of the incident laser radiation over a molecular absorption line [71, 72]. In this case, one can record either the output of an angular split (Figs. 2.6 and 2.8) or a differential measurement (Fig. 2.10) as a function of frequency, and the outcome of such an experiment would be the molecular spectrum of a chiral molecule through angle-resolved CHISPR measurements. Furthermore, in a SPR-based chiral-sensing scheme the whole evanescent-wave volume is sensitive to the probed chiral substance (due to the mobility of the propagating SPPs), contrary to contemporary chiral-sensing nanophotonic schemes that typically rely on localised surface plasmons, where the sign and magnitude of the chiroptical response can possess a complex dependence on sample geometry [26–31, 73]. Crucially, the CHISPR signals we demonstrate are within the sensitivity of current SPR instrumentation for the realistic values of the chirality parameter we consider and, therefore, CHISPR measurements can be directly realized on existing SPR measurement instrumentations with slight modifications on the analysis stage. As a final remark, we wish to emphasize here that since the observed relationships between κ and the measured quantities ($\Delta\theta$, ρ_{DR} and ϕ_{DR}) will effectively impose a lower limit of chiral detection, we expect that this can be further improved by enhancing the local fields, for

example via modification of the thin metal layer, e.g. via perforation, in order to take advantage of the strong evanescent fields at the gaps.

In overall, we expect our findings to be of great interest for chiral-biosensing applications, considering also that an angle-resolved CHISPR sensing scheme is a surface-sensitive measurement and differs from conventional chiral-sensing techniques based on transmission measurements. Crucially, the CHISPR scheme and its predicted signals we demonstrate are within, respectively, the capabilities and sensitivity of current SPR instrumentation and, therefore, CHISPR measurements it can be directly realized on existing SPR measurement instrumentations with slight modifications on the analysis stage. Furthermore, CHISR has also the potential for miniaturization and portable design [74–76] (we note here that recent developments in nanophotonics have unveiled novel ways to develop nanoscale Stokes polarimeters [77–79]), and such a possibility could enable compact devices for real-time sensing of biological processes that occur in limited regions of space

Acknowledgements We acknowledge the European Commission Horizon 2020, ULTRA-CHIRAL Project (grant no. FETOPEN-737071) for the financial support.

References

1. S.F. Mason, From Pasteur to parity violation: cosmic dissymmetry and the origins of biomolecular handedness. Ambix **38**(2), 85–108 (1991). https://doi.org/10.1179/amb.1991.38.2.85
2. S.F. Mason, Optical activity and molecular dissymmetry. Contemp. Phys. **9**(3), 239–256 (1968)
3. M. Levin, A.J.S. Klar, A.F. Ramsdell, Introduction to provocative questions in left–right asymmetry. Philos. Trans. R. Soc. B: Biol. Sci. **371**(1710), 20150399 (2016). https://doi.org/10.1098/rstb.2015.0399, https://royalsocietypublishing.org/doi/abs/10.1098/rstb.2015.0399
4. E.N. Fortson, L.L. Lewis, Atomic parity nonconservation experiments. Phys. Rep. **113(5)**(5), 289–344 (1984). https://doi.org/10.1016/0370-1573(84)90005-X, http://www.sciencedirect.com/science/article/pii/037015738490005X
5. G.D. Fasman, *Circular Dichroism and the Conformational Analysis of Biomolecules* (Springer US, New York, 2010)
6. S.M. Kelly, T.J. Jess, N.C. Price, How to study proteins by circular dichroism. Biochim. Biophys. Acta **1751**(2), 119–139 (2005). https://doi.org/10.1016/j.bbapap.2005.06.005, http://www.sciencedirect.com/science/article/pii/S1570963905001792
7. B. Nordén, A. Rodger, T. Dafforn, *Linear Dichroism and Circular Dichroism* (The Royal Society of Chemistry, London, 2010)
8. A.J. Hutt, S.C. Tan, Drug chirality and its clinical significance. Drugs **52**(5), 1–12 (1996). https://doi.org/10.2165/00003495-199600525-00003
9. Nguyen, L.A., He, H., Pham-Huy, C.: Chiral drugs: an overview. Int. J. Biomed. Sci. (IJBS) **2**(2), 85–100 (2006). https://www.ncbi.nlm.nih.gov/pubmed/23674971, https://www.ncbi.nlm.nih.gov/pmc/PMC3614593/
10. S. Droulias, L. Bougas, Surface plasmon platform for angle-resolved chiral sensing. ACS Photonics **6**(6), 1485–1492 (2019). https://doi.org/10.1021/acsphotonics.9b00137
11. L.D. Barron, *Molecular Light Scattering and Optical Activity*, 2 edn. (Cambridge University Press, Cambridge, 2004). https://doi.org/10.1017/CBO9780511535468
12. E.U. Condon, Theories of optical rotatory power. Rev. Mod. Phys. **9**, 432–457 (1937). https://doi.org/10.1103/RevModPhys.9.432, https://link.aps.org/doi/10.1103/RevModPhys.9.432

13. I.V. Lindell, A.H. Sihvola, S.A. Tretyakov, A.J. Viitanen, *Electromagnetic Waves in Chiral and Bi-isotropic Media* (Artech House, Norwood, 1994)
14. O. Arteaga, B. Kahr, Mueller matrix polarimetry of bianisotropic materials. J. Opt. Soc. Am. B **36**(8), F72–F83 (2019). https://doi.org/10.1364/JOSAB.36.000F72, http://josab.osa.org/abstract.cfm?URI=josab-36-8-F72
15. J.U. White, Long optical paths of large aperture. J. Opt. Soc. Am. **32**(5), 285–288 (1942). https://doi.org/10.1364/JOSA.32.000285, http://www.osapublishing.org/abstract.cfm?URI=josa-32-5-285
16. D. Herriott, H. Kogelnik, R. Kompfner, Off-axis paths in spherical mirror interferometers. Appl. Opt. **3**(4), 523–526 (1964). https://doi.org/10.1364/AO.3.000523, http://ao.osa.org/abstract.cfm?URI=ao-3-4-523
17. D. Das, A.C. Wilson, Very long optical path-length from a compact multi-pass cell. Appl. Phys. B **103**(3), 749–754 (2011). https://doi.org/10.1007/s00340-010-4337-7
18. K. Krzempek, M. Jahjah, R. Lewicki, P. Stefański, S. So, D. Thomazy, F.K. Tittel, CW DFB RT diode laser-based sensor for trace-gas detection of ethane using a novel compact multipass gas absorption cell. Appl. Phys. B **112**(4), 461–465 (2013). https://doi.org/10.1007/s00340-013-5544-9
19. T. Müller, K.B. Wiberg, P.H. Vaccaro, Cavity ring-down polarimetry (CRDP): a new scheme for probing circular birefringence and circular dichroism in the gas phase. J. Phys. Chem. A **104**(25), 5959–5968 (2000). https://doi.org/10.1021/jp000705n
20. T. Müller, K.B. Wiberg, P.H. Vaccaro, Cavity ring-down polarimetry (CRDP): a new scheme for probing circular birefringence and circular dichroism in the gas phase. J. Phys. Chem. A **104**(25), 5959–5968 (2000). https://doi.org/10.1021/jp000705n
21. T. Müller, K.B. Wiberg, P.H. Vaccaro, J.R. Cheeseman, M.J. Frisch, Cavity ring-down polarimetry (CRDP): theoretical and experimental characterization. J. Opt. Soc. Am. B **19**(1), 125–141 (2002). https://doi.org/10.1364/JOSAB.19.000125, http://josab.osa.org/abstract.cfm?URI=josab-19-1-125
22. L. Bougas, G.E. Katsoprinakis, W. von Klitzing, J. Sapirstein, T.P. Rakitzis, Cavity-enhanced parity-nonconserving optical rotation in metastable Xe and Hg. Phys. Rev. Lett. **108**, 210801 (2012). https://doi.org/10.1103/PhysRevLett.108.210801, https://link.aps.org/doi/10.1103/PhysRevLett.108.210801
23. D. Sofikitis, L. Bougas, G.E. Katsoprinakis, A.K. Spiliotis, B. Loppinet, T.P. Rakitzis, Evanescent-wave and ambient chiral sensing by signal-reversing cavity ringd-own polarimetry. Nature **514**, 76 (2014). https://doi.org/10.1038/nature13680, http://10.0.4.14/nature13680
24. L. Bougas, D. Sofikitis, G.E. Katsoprinakis, A.K. Spiliotis, P. Tzallas, B. Loppinet, T.P. Rakitzis, Chiral cavity ring down polarimetry: chirality and magnetometry measurements using signal reversals. J. Chem. Phys. **143**(10), 104202 (2015). https://doi.org/10.1063/1.4930109
25. G.E. Katsoprinakis, L. Bougas, T.P. Rakitzis, V.A. Dzuba, V.V. Flambaum, Calculation of parity-nonconserving optical rotation in iodine at 1315 nm. Phys. Rev. A **87**, 040101 (2013). https://doi.org/10.1103/PhysRevA.87.040101, https://link.aps.org/doi/10.1103/PhysRevA.87.040101
26. E. Hendry, T. Carpy, J. Johnston, M. Popland, R.V. Mikhaylovskiy, A.J. Lapthorn, S.M. Kelly, L.D. Barron, N. Gadegaard, M. Kadodwala, Ultrasensitive detection and characterization of biomolecules using superchiral fields. Nat. Nanotechnol. **5**, 783 (2010)
27. Y. Tang, A.E. Cohen, Enhanced enantioselectivity in excitation of chiral molecules by superchiral light. Science **332**(6027), 333–336 (2011). https://doi.org/10.1126/science.1202817
28. T.J. Davis, E. Hendry, Superchiral electromagnetic fields created by surface plasmons in nonchiral metallic nanostructures. Phys. Rev. B **87**, 085405 (2013). https://doi.org/10.1103/PhysRevB.87.085405
29. A.S. Karimullah, C. Jack, R. Tullius, V.M. Rotello, G. Cooke, N. Gadegaard, L.D. Barron, M. Kadodwala, Disposable plasmonics: plastic templated plasmonic metamaterials with tunable chirality. Adv. Mater. **27**(37), 5610–5616 (2015). https://doi.org/10.1002/adma.201501816
30. Y. Luo, C. Chi, M. Jiang, R. Li, S. Zu, Y. Li, Z. Fang, Plasmonic chiral nanostructures: chiroptical effects and applications. Adv. Opt. Mater. **5**(16), 1700040 (2017). https://doi.org/10.1002/adom.201700040

31. Y. Zhao, A.N. Askarpour, L. Sun, J. Shi, X. Li, A. Alù, Chirality detection of enantiomers using twisted optical metamaterials. Nat. Commun. **8**, 14180 (2017)
32. E. Mohammadi, K.L. Tsakmakidis, A.N. Askarpour, P. Dehkhoda, A. Tavakoli, H. Altug, Nanophotonic platforms for enhanced chiral sensing. ACS Photonics **5**(7), 2669–2675 (2018). https://doi.org/10.1021/acsphotonics.8b00270
33. M.L. Solomon, J. Hu, M. Lawrence, A. García-Etxarri, J.A. Dionne, Enantiospecific optical enhancement of chiral sensing and separation with dielectric metasurfaces. ACS Photonics **6**(1), 43–49 (2019). https://doi.org/10.1021/acsphotonics.8b01365
34. N.A. Abdulrahman, Z. Fan, T. Tonooka, S.M. Kelly, N. Gadegaard, E. Hendry, A.O. Govorov, M. Kadodwala, Induced chirality through electromagnetic coupling between chiral molecular layers and plasmonic nanostructures. Nano Lett. **12**(2), 977–983 (2012). https://doi.org/10.1021/nl204055r
35. C. Kelly, L. Khosravi Khorashad, N. Gadegaard, L.D. Barron, A.O. Govorov, A.S. Karimullah, M. Kadodwala, Controlling metamaterial transparency with superchiral fields. ACS Photonics **5**(2), 535–543 (2018).https://doi.org/10.1021/acsphotonics.7b01071
36. J. García-Guirado, M. Svedendahl, J. Puigdollers, R. Quidant, Enhanced chiral sensing with dielectric nanoresonators. Nano Lett. **20**(1), 585–591 (2020). https://doi.org/10.1021/acs.nanolett.9b04334. PMID: 31851826
37. S. Droulias, Chiral sensing with achiral isotropic metasurfaces. Phys. Rev. B **102**, 075119 (2020). https://doi.org/10.1103/PhysRevB.102.075119, https://link.aps.org/doi/10.1103/PhysRevB.102.075119
38. H.H. Nguyen, J. Park, S. Kang, M. Kim, Surface plasmon resonance: a versatile technique for biosensor applications. Sensors **15**(5), 10481–10510 (2015). https://doi.org/10.3390/s150510481
39. R.B.M. Schasfoort (ed.), *Handbook of Surface Plasmon Resonance* (The Royal Society of Chemistry, London, 2017). https://doi.org/10.1039/9781788010283
40. E. Kretschmann, Decay of non radiative surface plasmons into light on rough silver films. comparison of experimental and theoretical results. Opt. Commun. **6**(2), 185–187 (1972). https://doi.org/10.1016/0030-4018(72)90224-6, http://www.sciencedirect.com/science/article/pii/0030401872902246
41. H. Raether, *Surface Plasmons on Smooth and Rough Surfaces and on Gratings*. Springer Tracts in Modern Physics (Springer, Berlin, 1988). https://doi.org/10.1007/BFb0048317, https://www.springer.com/gp/book/9783662151242
42. S.A. Maier, *Plasmonics: Fundamentals and Applications* (Springer US, New York, 2007). https://doi.org/10.1007/0-387-37825-1, https://www.springer.com/gp/book/9780387331508
43. L. Novotny, B. Hecht, *Principles of Nano-Optics*, 2 edn. (Cambridge University Press, Cambridge, 2012). https://doi.org/10.1017/CBO9780511794193, https://www.cambridge.org/core/books/principles-of-nanooptics/E884E5F4AA76DF179A1ECFDF77436452
44. E.N. Economou, Surface plasmons in thin films. Phys. Rev. **182**(2), 539–554 (1969). https://doi.org/10.1103/PhysRev.182.539
45. J.J. Burke, G.I. Stegeman, T. Tamir, Surface-polariton-like waves guided by thin, lossy metal films. Phys. Rev. B **33**(8), 5186–5201 (1986). https://doi.org/10.1103/PhysRevB.33.5186
46. P. Berini, Plasmon-polariton waves guided by thin lossy metal films of finite width: bound modes of symmetric structures. Phys. Rev. B **61**(15), 10484–10503 (2000). https://doi.org/10.1103/PhysRevB.61.10484
47. W.L. Barnes, A. Dereux, T.W. Ebbesen, Surface plasmon subwavelength optics. Nature **424**(6950), 824–830 (2003). https://doi.org/10.1038/nature01937
48. W.L. Barnes, Surface plasmon-polariton length scales: a route to sub-wavelength optics. J. Opt. A: Pure Appl. Opt. **8**(4), S87–S93 (2006). https://doi.org/10.1088/1464-4258/8/4/S06
49. J.M. Pitarke, V.M. Silkin, E.V. Chulkov, P.M. Echenique, Theory of surface plasmons and surface-plasmon polaritons. Rep. Prog. Phys. **70**(1), 1–87 (2006). https://doi.org/10.1088/0034-4885/70/1/R01
50. B. Dastmalchi, P. Tassin, T. Koschny, C.M. Soukoulis, A new perspective on plasmonics: confinement and propagation length of surface plasmons for different materials and geometries. Adv. Opt. Mater. **4**(1), 177–184 (2016). https://doi.org/10.1002/adom.201500446

51. G. Mi, V. Van, Characteristics of surface plasmon polaritons at a chiral-metal interface. Opt. Lett. **39**(7), 2028–2031 (2014). https://doi.org/10.1364/OL.39.002028
52. P. Pelet, N. Engheta, The theory of chirowaveguides. IEEE Trans. Antennas Propag. **38**(1), 90–98 (1990). https://doi.org/10.1109/8.43593
53. P.B. Johnson, R.W. Christy, Optical constants of the noble metals. Phys. Rev. B **6**, 4370–4379 (1972). https://doi.org/10.1103/PhysRevB.6.4370
54. S.A. Maier, H.A. Atwater, Plasmonics: localization and guiding of electromagnetic energy in metal/dielectric structures. J. Appl. Phys. **98**(1), 011101 (2005). https://doi.org/10.1063/1.1951057
55. K. Zhelyazkova, M. Petrov, B. Katranchev, G. Dyankov, Surface plasmon resonance on the surface: metal - liquid crystal layer. J. Phys.: Conf. Ser. **558**, 012023 (2014). https://doi.org/10.1088/1742-6596/558/1/012023
56. M. Wang, H. Li, T. Xu, H. Zheng, M. Yu, G. Li, J. Xu, J. Wu, Probing bianisotropic biomolecules via a surface plasmon resonance sensor. Opt. Express **26**(22), 28277–28287 (2018). https://doi.org/10.1364/OE.26.028277
57. L.V. Poulikakos, P. Thureja, A. Stollmann, E. De Leo, D.J. Norris, Chiral light design and detection inspired by optical antenna theory. Nano Lett. **18**(8), 4633–4640 (2018). https://doi.org/10.1021/acs.nanolett.8b00083. PMID: 29533637
58. M.P. Silverman, J. Badoz, B. Briat, Chiral reflection from a naturally optically active medium. Opt. Lett. **17**(12), 886–888 (1992). https://doi.org/10.1364/OL.17.000886
59. M. Silverman, J. Badoz, Large enhancement of chiral asymmetry in light reflection near critical angle. Opt. Commun. **74**(3), 129–133 (1989)
60. M. Piliarik, J. Homola, Surface plasmon resonance (SPR) sensors: approaching their limits? Opt. Express **17**(19), 16505–16517 (2009). https://doi.org/10.1364/OE.17.016505
61. X. Wang, M. Jefferson, P.C.D. Hobbs, W.P. Risk, B.E. Feller, R.D. Miller, A. Knoesen, Shot-noise limited detection for surface plasmon sensing. Opt. Express **19**(1), 107–117 (2011). https://doi.org/10.1364/OE.19.000107
62. R.C. Pooser, B. Lawrie, Plasmonic trace sensing below the photon shot noise limit. ACS Photonics **3**(1), 8–13 (2016). https://doi.org/10.1021/acsphotonics.5b00501
63. A.V. Kabashin, S. Patskovsky, A.N. Grigorenko, Phase and amplitude sensitivities in surface plasmon resonance bio and chemical sensing. Opt. Express **17**(23), 21191–21204 (2009). https://doi.org/10.1364/OE.17.021191
64. S. Patskovsky, M. Meunier, P.N. Prasad, A.V. Kabashin, Self-noise-filtering phase-sensitive surface plasmon resonance biosensing. Opt. Express **18**(14), 14353–14358 (2010). https://doi.org/10.1364/OE.18.014353
65. D.M. Lipkin, Existence of a new conservation law in electromagnetic theory. J. Math. Phys. **5**(5), 696–700 (1964). https://doi.org/10.1063/1.1704165
66. Y. Tang, A.E. Cohen, Optical chirality and its interaction with matter. Phys. Rev. Lett. **104**, 163901 (2010). https://doi.org/10.1103/PhysRevLett.104.163901, https://link.aps.org/doi/10.1103/PhysRevLett.104.163901
67. K.Y. Bliokh, F. Nori, Characterizing optical chirality. Phys. Rev. A **83**, 021803 (2011). https://doi.org/10.1103/PhysRevA.83.021803
68. M.M. Coles, D.L. Andrews, Chirality and angular momentum in optical radiation. Phys. Rev. A **85**, 063810 (2012). https://doi.org/10.1103/PhysRevA.85.063810
69. T.G. Philbin, Lipkin's conservation law, Noether's theorem, and the relation to optical helicity. Phys. Rev. A **87**, 043843 (2013). https://doi.org/10.1103/PhysRevA.87.043843, https://link.aps.org/doi/10.1103/PhysRevA.87.043843
70. L.V. Poulikakos, P. Gutsche, K.M. McPeak, S. Burger, J. Niegemann, C. Hafner, D.J. Norris, Optical chirality flux as a useful far-field probe of chiral near fields. ACS Photonics **3**(9), 1619–1625 (2016). https://doi.org/10.1021/acsphotonics.6b00201
71. A. Ikehata, T. Itoh, Y. Ozaki, Surface plasmon resonance near-infrared spectroscopy. Anal. Chem. **76**(21), 6461–6469 (2004). https://doi.org/10.1021/ac049003a
72. R. Zektzer, L. Stern, N. Mazurski, U. Levy, Enhanced light-matter interactions in plasmonic-molecular gas hybrid system. Optica **5**(4), 486–494 (2018). https://doi.org/10.1364/OPTICA.5.000486, http://www.osapublishing.org/optica/abstract.cfm?URI=optica-5-4-486

73. Y. Tang, L. Sun, A.E. Cohen, Chiroptical hot spots in twisted nanowire plasmonic oscillators. Appl. Phys. Lett. **102**(4), 043103 (2013). https://doi.org/10.1063/1.4789529
74. P. Preechaburana, M.C. Gonzalez, A. Suska, D. Filippini, Surface plasmon resonance chemical sensing on cell phones. Angew. Chem. Int. Ed. **51**(46), 11585–11588 (2012). https://doi.org/10.1002/anie.201206804, https://onlinelibrary.wiley.com/doi/abs/10.1002/anie.201206804
75. Y. Liu, Q. Liu, S. Chen, F. Cheng, H. Wang, W. Peng, Surface plasmon resonance biosensor based on smart phone platforms. Sci. Rep. **5**, 12864 (2015). https://doi.org/10.1038/srep12864, http://10.0.4.14/srep12864
76. H. Guner, E. Ozgur, G. Kokturk, M. Celik, E. Esen, A.E. Topal, S. Ayas, Y. Uludag, C. Elbuken, A. Dana, A smartphone based surface plasmon resonance imaging (SPRI) platform for on-site biodetection. Sens. Actuators B: Chem. **239**, 571–577 (2017). https://doi.org/10.1016/j.snb.2016.08.061, http://www.sciencedirect.com/science/article/pii/S092540051631293X
77. J.P.B. Mueller, K. Leosson, F. Capasso, Ultracompact metasurface in-line polarimeter. Optica **3**(1), 42–47 (2016). https://doi.org/10.1364/OPTICA.3.000042, http://www.osapublishing.org/optica/abstract.cfm?URI=optica-3-1-42
78. A. Espinosa-Soria, F.J. Rodríguez-Fortuño, A. Griol, A. Martínez, On-chip optimal stokes nanopolarimetry based on spin-orbit interaction of light. Nano Lett. **17**, 3139–3144 (2017). https://doi.org/10.1021/acs.nanolett.7b00564
79. P.C. Wu, J.W. Chen, C.W. Yin, Y.C. Lai, T.L. Chung, C.Y. Liao, B.H. Chen, K.W. Lee, C.J. Chuang, C.M. Wang, D.P. Tsai, Visible metasurfaces for on-chip polarimetry. ACS Photonics **5**(7), 2568–2573 (2018). https://doi.org/10.1021/acsphotonics.7b01527